Modeling wave impact on salt marsh boundaries

Mara Tonelli,[1,2] Sergio Fagherazzi,[2] and Marco Petti[1]

Received 1 December 2009; revised 14 April 2010; accepted 13 May 2010; published 29 September 2010.

[1] Wind-wave attack is the fundamental cause of erosion of salt marsh boundaries. Tidal forcing acts as a proxy determining at which elevation waves pound against the marsh edge and conditioning the propagation and transformation of wave trains as they move toward these boundaries. The objective of the present work is to evaluate, through analysis of the results of a numerical model, the effect of wave action on marsh boundaries as a function of tidal elevation and wave height for different edge configurations. In order to link numerical simulations to field conditions, the model inputs are based on topographical and hydrodynamical surveys conducted at a study site at the Virginia Coast Reserve (VCR), VA. Model results show that the wave thrust on the marsh scarp strongly depends on tidal level. The thrust increases with tidal elevation until the marsh is submerged and then rapidly decreases. The wave thrust is maximum for a vertical scarp and minimum for a terraced scarp. Similarly, wave energy dissipation is maximized just above the marsh platform elevation, when wave reflection is reduced and wave breaking occurs at the marsh edge.

Citation: Tonelli, M., S. Fagherazzi, and M. Petti (2010), Modeling wave impact on salt marsh boundaries, *J. Geophys. Res.*, *115*, C09028, doi:10.1029/2009JC006026.

1. Introduction

[2] Coastal wetlands and salt marshes are among the richest ecosystems in terms of productivity and species diversity, providing a habitat to a diverse animal population, valuable resources for fishing and recreation, and nutrient recycling. Salt marshes are also important for flood prevention, as they efficiently dissipate wind-wave and tidal energy [*Möller and Spencer*, 2002], thus reducing the dimensions of defense structures built at their landward limit, with relevant economic advantages [*King and Lester*, 1995].

[3] Despite their manifold significance, salt marshes are experiencing considerable surface loss in numerous locations: along the mid-Atlantic coast in the United States [*Day et al.*, 2000; *Schwimmer*, 2001], in northwestern Europe [*Allen*, 2000; *van der Wal and Pye*, 2004], and in southern Asia [*Edinger and Browne*, 2000].

[4] Salt marsh survival depends on a delicate balance between the processes supporting marsh thriving (e.g., vertical accretion and vegetation colonization) and those endangering it, such as surface degradation and margin erosion. The rate of relative sea level rise, the tidal regime, the wind-wave climate, the sediment supply, and the development of a vegetation cover are fundamental driving forces for salt marsh evolution [*Temmerman et al.*, 2004; *D'Alpaos et al.*, 2005; *Fagherazzi and Sun*, 2004; *Fagherazzi and Overeem*, 2007; *Mariotti and Fagherazzi*, 2010]. Of critical importance are also the dynamics taking place at the boundary between salt marshes and tidal flats. Both landforms are inherently flat and subject to sedimentary and erosive processes: tidal flats conservation results from the balance between sediment deposition and resuspension by wind waves and tidal currents [*Allen and Duffy*, 1998; *Fagherazzi et al.*, 2006, 2007; *Defina et al.*, 2007], while salt marsh evolution is closely related to its elevation, which is controlled by mineral and organogenic sediment accumulation [*Pethick*, 1981; *Fagherazzi and Furbish*, 2001; *D'Alpaos et al.*, 2006], sea level elevation, and the stabilizing effect of halophyte vegetation on its platform [*Morris et al.*, 2002; *Mudd et al.*, 2004; *Silvestri et al.*, 2005; *Kirwan and Murray*, 2007].

[5] The evolution of the two landforms is closely related: marsh deterioration is generally linked to the erosion and collapse of the marsh edges under wind waves [*Möller et al.*, 1999; *Möller*, 2006; *van de Koppel et al.*, 2005] and the elevation of tidal flats bordering the marsh platform together with fetch distances strongly influence the energy level of the incoming waves and the energy dissipated at the marsh margin, thus determining erosion rates [*Mariotti and Fagherazzi*, 2010; *Möller et al.*, 2009].

[6] Because of morphological and biological gradients, the boundary dividing tidal flats and salt marshes is often characterized by a distinct scarp [*van de Koppel et al.*, 2005; *Mariotti and Fagherazzi*, 2010] whose vertical profile is an indicator of the prevalence of accretion or erosion [*Kirby*, 2000]: accreting shores are often convex while erosion-dominated shores are concave so that the edge between the tidal flat and the backing salt marsh assumes the shape of a cliff [*Mariotti and Fagherazzi*, 2010]. Cliffs may also result from autogenic marsh formation. The marsh cliff forms as a

[1]Dipartimento di Georisorse e Territorio, Università degli Studi di Udine, Udine, Italy.
[2]Department of Earth Sciences and Center for Computational Science, Boston University, Boston, Massachusetts, USA.

0148-0227/10/2009JC006026

result of mudflat accretion, which increases the proportion of the intertidal landscape that is at high elevations and moves the marsh-mudflat transition seaward, thus exposing this transition to higher wave energy levels [*Pethick*, 1981; *Allen*, 2000; *van de Koppel et al.*, 2005]. However, it should be noted that cliff formation is only one of the possible responses of marsh margins to wind wave erosion: other retreating behaviors exist (e.g., marsh edge dissection, creek widening, creek bank erosion, mud-mound topography formation) [e.g., *Allen*, 2000; *van der Wal and Pye*, 2004].

[7] A typical style of edge erosion is cliff undercutting: the lower mud layer is eroded more rapidly than the overlying rootmat, leading to the formation of an overhang, which eventually falls at the foot of the scarp or is thrown over the platform by waves hitting the marsh. Evidence of this kind of erosional process is given by the presence of salt marsh blocks degrading to mud balls at the scarp base and on the marsh platform. An alternative marsh edge configuration consists of the formation of a step-like profile, with a lower steep scarp, followed by a short, mildly sloping terrace and a higher, almost vertical cliff leading to the marsh platform. Other types of marsh edge configuration common elsewhere (e.g., multiple terraces due to sea level change [*Allen*, 1990]) have not been detected at our study site.

[8] Wind-wave attack is recognized as the fundamental agent of salt marsh erosion [*Feagin*, 2008; *Barbier et al.*, 2008], particularly in microtidal basins or sheltered back-barrier areas; tidal conditions act as a proxy determining the elevation at which waves pound against the marsh edge and conditioning the propagation and transformation of wave trains as they move toward these boundaries.

[9] The objective of the present work is to evaluate, through analysis of the results of a numerical model, the effect of wave action on marsh boundaries as a function of tidal elevation and wave height for different edge configurations.

[10] A numerical Boussinesq-type model is applied to simulate wave train propagation against and over three configurations of marsh boundaries (a vertical bank, sloping scarp, and terraced edge) under different tidal and wave conditions and compute the thrust exerted by waves on such boundaries and the related energy dissipation. In order to link numerical simulations to field conditions, the model inputs (bathymetries, wave train parameters, tidal levels) are based on topographical and hydrodynamical surveys conducted at a study site at the Virginia Coast Reserve. The results for the three cases are compared and discussed.

2. Numerical Model

2.1. Wave Model

[11] The wave model is based on the coupled solution of Boussinesq and nonlinear shallow water equations (NSWE); both are depth-averaged approximations to the 3-D mass and momentum conservation equations for an incompressible, nonviscid flow.

[12] Boussinesq equations are derived by accounting for the nonhydrostatic effect of vertical particle acceleration on pressure distribution and can describe both the nonlinear and frequency-dispersive features of wave propagation. The applicability of classical Boussinesq equations [*Peregrine*, 1967] is restricted to weakly nonlinear and weakly dispersive shallow water flows. To overcome such limitation, several alternative formulations with improved dispersive and nonlinear properties were developed (for a review, see *Madsen and Schäffer* [1999] and *Kirby* [2003]). Further studies were devoted to extending the applicability of Boussinesq-type models to surf zone waves. Specific algorithms were developed to represent the shoreline movement [*Zelt*, 1991; *Madsen et al.*, 1997; *Lynett et al.*, 2002]. Wave breaking was artificially incorporated by adding ad hoc terms, which account for its effects on the flow and can be calculated in different ways [*Karambas and Koutitas*, 1992; *Schäffer et al.*, 1993; *Veeramony and Svendsen*, 2000; *Karambas and Tozer*, 2003]. Whatever technique is used, a number of calibrated parameters is always introduced and a certain amount of arbitrariness cannot be avoided. Moreover, the application of all the aforementioned techniques becomes rather complex when 2-D domains are considered. Such artificial and complicated treatment of wave breaking and shoreline motion is one of the major shortcomings of Boussinesq models.

[13] NSWE are a nondispersive subset of Boussinesq-type equations; the pressure is assumed to be hydrostatic and the flow conditions are dominated by advection. Because of the lack of dispersion, NSWE cannot describe short-wave propagation, but they can be applied to very long waves or to situations where nonlinear effects prevail, such as in the inner surf zone and at the shore [*Hibberd and Peregrine*, 1979; *Kobayashi et al.*, 1989; *Watson and Peregrine*, 1992]. The main advantage of NSWE is that, when integrated by means of shock-capturing methods, they naturally embody flow propagation on a dry bed, bore formation and propagation, and the related energy loss [*Toro*, 2001]. Therefore, NSWE can intrinsically model shoreline motion [*Brocchini et al.*, 2001] and, given the similarity of bores and spilling breakers [*Peregrine and Svendsen*, 1978; *Basco and Svendsen*, 1984], wave breaking, at least of spilling type.

[14] The wave model applied in this work combines the best features of the two systems of equations: the propagation properties of Boussinesq-type equations and the shock-capturing features of NSWE, solving Boussinesq equations where nonlinear and dispersive effects are about the same order and applying NSWE when dispersion is negligible and nonlinearity prevails.

2.1.1. Governing Equations

[15] The governing Boussinesq equations [*Madsen and Sørensen*, 1992, hereafter MS92], formulated in conservative form, are given as follows:

$$\begin{bmatrix} h \\ P \\ Q \end{bmatrix}_t + \begin{bmatrix} P \\ P^2/h + gh^2/2 \\ PQ/h \end{bmatrix}_x + \begin{bmatrix} Q \\ PQ/h \\ Q^2/h + gh^2/2 \end{bmatrix}_y + \begin{bmatrix} 0 \\ ghz_x + \psi_1 + \tau_x/\rho \\ ghz_y + \psi_2 + \tau_y/\rho \end{bmatrix} = 0 \quad (1)$$

where subscripts x, y, and t denote differentiation with reference to space and time; h is the total water depth; P and Q are the volume fluxes; z is the bottom elevation measured from a fixed datum (Figure 1); g is the gravitational acceleration; τ_x and τ_y are the bottom friction terms; ρ is the

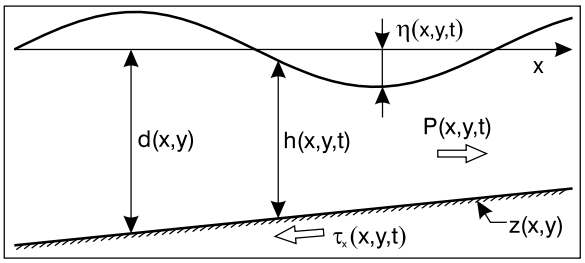

Figure 1. Symbols used in the formulation of Boussinesq equations.

water density; and ψ_1 and ψ_2 indicate the modified dispersive terms defined by:

$$\psi_1 = -\left(B+\frac{1}{3}\right)d^2\left(P_{xxt}+Q_{xyt}\right) - Bgd^3\left(\eta_{xxx}+\eta_{xyy}\right) - \frac{1}{3}dd_xP_{xt} - \frac{1}{6}dd_xQ_{yt} - Bgd^2d_x\left(2\eta_{xx}+\eta_{yy}\right) - dd_y\left(\frac{1}{6}Q_{xt}+Bgd\eta_{xy}\right)$$

$$\psi_2 = -\left(B+\frac{1}{3}\right)d^2\left(P_{xyt}+Q_{yyt}\right) - Bgd^3\left(\eta_{yyy}+\eta_{yxx}\right) - \frac{1}{3}dd_yQ_{yt} - \frac{1}{6}dd_yP_{xt} - Bgd^2d_y\left(2\eta_{yy}+\eta_{xx}\right) - dd_x\left(\frac{1}{6}P_{yt}+Bgd\eta_{xy}\right) \quad (2)$$

where d is the still water depth, η is the water surface elevation, and B is a calibration coefficient, determining the dispersion properties of the equations. Here the value $B = 1/15$ has been adopted, as suggested by *Madsen et al.* [1991]. When dispersive terms in equation (1) are dropped, NSWE are recovered.

[16] Neglecting its time-varying structure, the bed shear stress is frequently given by the quadratic law:

$$\begin{bmatrix}\tau_x/\rho\\ \tau_y/\rho\end{bmatrix} = \frac{f_w}{2}\begin{bmatrix}P\\ Q\end{bmatrix}\frac{\sqrt{P^2+Q^2}}{h^2} \quad (3)$$

where f_w is the friction factor, depending on the Reynolds number and the seafloor conditions. The evaluation of the friction factor is complex and subject to some amount of uncertainty. In a salt marsh environment, the friction factor has significant spatial variations: on the tidal flat, typical values for sand are around 0.01; on the platform, the friction factor value depends on the characteristics of the vegetation covering the surface. Estimates of the friction factor are reported to range from 0.07 to 0.47 for thick stands of marsh grass [*Department of the Army, Waterways Experiment Station, Corps of Engineers, and Coastal Engineering Research Center*, 1984].

[17] In this study, the effect of vegetation on the flow is globally represented by suitably assigning the friction factor instead of modeling wave interaction with marsh vegetation. This choice was made because the aim of the present study is to evaluate wave action on the marsh edge, therefore wave characteristics on the platform are computed close to the edge (2.5–4 m); over such short distances, and for the purposes of concentrating modeling efforts on the interaction of waves with the scarp face, the effect of vegetation on waves is assumed to be small. Moreover, wave breaking, when it occurs, is the main source of energy dissipation over the first meters of the platform, whereas the effect of vegetation is secondary. Bed shear stresses are evaluated assigning a friction factor $f_w = 0.01$ to the tidal flat area and a friction factor $f_w = 0.1$ to the platform.

2.1.2. Numerical Scheme

[18] The governing equations are integrated numerically applying the finite volume method (FVM); however, because of the presence of high-order derivatives in the dispersive terms (2), this cannot be done straightforwardly. Hence, following the work of *Erduran et al.* [2005], a hybrid procedure is applied. The advective part of the equations is solved explicitly employing the FVM, while dispersive and bottom slope terms are treated as source terms and discretized using the finite difference method.

[19] Advective fluxes are calculated by applying the HLL Riemann solver [*Toro*, 2001] coupled with a MUSCL-TVD algorithm to achieve fourth-order accuracy. Data construction and the discretization of bottom slope terms are performed following the surface gradient method [*Zhou et al.*, 2001]. The remaining terms are simply treated by centered finite differencing.

[20] Time integration is performed applying the fourth-order predictor-corrector method introduced in Boussinesq models by *Wei and Kirby* [1995]. The total water depth h is calculated explicitly from the continuity equation, whereas the fluxes P and Q are evaluated implicitly. Details on the numerical procedure can be found in the work of *Tonelli and Petti* [2009]. Attention is focused here only on the aspects relevant to the present application.

2.1.2.1. Wave Breaking

[21] The proposed approach to wave breaking modeling is based on the following considerations: when waves approach the breaking condition, they undergo a transformation getting higher and steeper, therefore nonlinear effects become more important than dispersive effects. At breaking, dispersion is negligible compared to nonlinearity and NSWE become a reasonable approximation of the flow conditions.

[22] Following the evolution of the waves, Boussinesq equations are applied where nonlinear and dispersive terms are about the same order and NSWE where nonlinearity predominates over dispersion. A criterion is introduced in the scheme to establish where and when the conditions for the application of NSWE are satisfied. As noted by *Okamoto and Basco* [2006], the transition from nonbreaking to breaking waves is analogous to the transition from undular to fully developed, turbulent bores, a transition known to occur in a specific range of Froude number (F_r) values [*Chanson and Montes*, 1995]. Given the similarity of bores and breakers [*Peregrine and Svendsen*, 1978] and the fact that undular bores are well modeled by Boussinesq equations [*Peregrine*, 1966; *Soares Frazão and Zech*, 2002] and turbulent bores by NSWE [*Hu et al.*, 1998], we decided to base the criterion for switching from Boussinesq to NSWE on the overcoming of a threshold Froude number value. However, since tracking the Froude number is numerically inconvenient, we adopted a threshold on the relative wave height $\varepsilon = H/d$ (see *Tonelli and Petti* [2009] for details). The limiting condition for the formation of a fully developed bore $F_r = 1.60$ [*Chanson and Montes*, 1995] corresponds to $\varepsilon = 0.8$. At every time step, the value of ε is computed cell by cell: if it is lower than 0.8, Boussinesq equations are applied, otherwise NSWE are used. Once NSWE are applied,

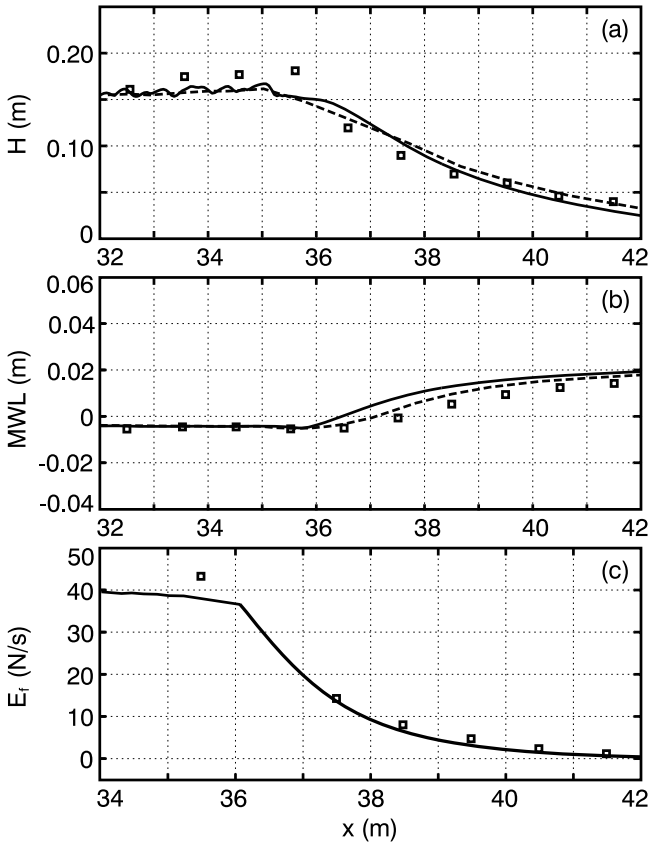

Figure 2. Wave breaking on a plane slope: spatial variation of the (a) mean wave height, (b) mean water level, and (c) time-averaged energy flux. Symbols, experimental data [*Stive*, 1980]; solid line, present model results; dashed line, solution of *Madsen et al.* [1997]. Adapted from *Tonelli and Petti* [2009].

the evolution of the breaker and the resulting wave height decay stem automatically from the solution of the NSWE, therefore no dissipation terms need to be added to the equations and arbitrariness is reduced with respect to other existing breaking models. Further details on the breaking model can be found in the work of *Tonelli and Petti* [2009, 2010].

2.1.2.2. Boundary Conditions

[23] Four kinds of boundary conditions are used in the present study. A wavemaker boundary condition is imposed assigning all the variables (h, P, Q) at the offshore boundary of the domain. In this study, given the test conditions, the second-order Stokes theory is used to calculate the water depth and the fluxes from the incident wave height and period. This kind of condition does not allow the treatment of reflected waves arriving from the domain back at the boundary; therefore, the time intervals for the analysis of the numerical outputs are suitably selected to avoid the influence in the area of study of waves re-reflected from the generation boundary. For each test case, the time series of water surface elevation at the seaward section of the study area are examined to visually detect the arrival time of re-reflected waves (t_a); the closing time of the window used for data analysis is then set a wave period earlier than t_a. The starting time is set at the instant when the flow has reached an averagely stationary condition over the whole length of the area of study and it is determined by observing the time series of surface elevation at the landward section of the area of study.

[24] At fully reflective boundaries, the normal flux and the gradient of the water surface must be zero, thus the boundary condition can be stated as:

$$(P, Q) \cdot \mathbf{n} = 0 \text{ and } \nabla h \cdot \mathbf{n} = 0 \tag{4}$$

where $\mathbf{n}$ is the outward unit normal vector of the boundary.

[25] Absorbing conditions are meant to perfectly dissipate all the energy carried by the disturbances approaching the boundary from within the domain in order to eliminate unphysical reflections. In front of this kind of boundaries a damping region is defined; on it, the values of surface elevation and fluxes are progressively reduced by multiplication for a coefficient $\alpha(x, y)$ calculated as follows:

$$\alpha(x,y) = \begin{cases} 0.5 + 0.5\cos\left(\pi \dfrac{L_s}{L_s - D(x,y)}\right) & D \le L_s \\ 1 & D > L_s \end{cases} \tag{5}$$

where L_s is the width of the damping region and $D(x, y)$ is the normal distance between the cell center of coordinates (x, y) and the boundary.

[26] The application of the FVM for the solution of the advective part of the governing equations gives the numerical scheme the capability to treat the shoreline motion intrinsically [*Tonelli and Petti*, 2010]. The propagation on a dry bed is automatically handled when the Riemann problem is solved at cell interfaces. A threshold is introduced to locate the wet-dry interface: if the total water depth at a cell center is greater than the threshold, the wet bed solution of the Riemann problem is applied; otherwise the dry bed case is used.

2.1.3. Validation for the Present Application

[27] This section deals with two aspects of the proposed numerical modeling that are relevant for the applications presented in this study: the dissipation of energy and the interaction with steep bottom slopes. Since the wave breaking module has been extensively validated [*Tonelli and Petti*, 2009, 2010], only an example of energy calculation is reported here. To verify the performance of the present numerical model over steep bottom slopes, two benchmark test cases of partial wave reflection on a plane shelf and a case of solitary wave interaction with a rectangular step are proposed.

[28] The numerical model is applied to reproduce one of the experimental tests conducted by *Stive* [1980] to study waves breaking on a gently sloping beach. The numerical domain is 55 m long; a 16 m long, constant depth (d = 0.7 m) section is followed by a plane beach of slope 1/40. The grid size is Δx = 0.05 m, the time step is Δt = 0.005 s. A wavemaker boundary condition is imposed at the left end of the domain to generate second-order Stokes waves with a period T = 1.79 s and wave height H_0 = 0.156 m. At the opposite end the moving shoreline is modeled, therefore no specific algorithm is required.

[29] Figures 2a and 2b show the spatial evolution of the wave height and mean water level (MWL); the proposed numerical results are plotted against the experimental data

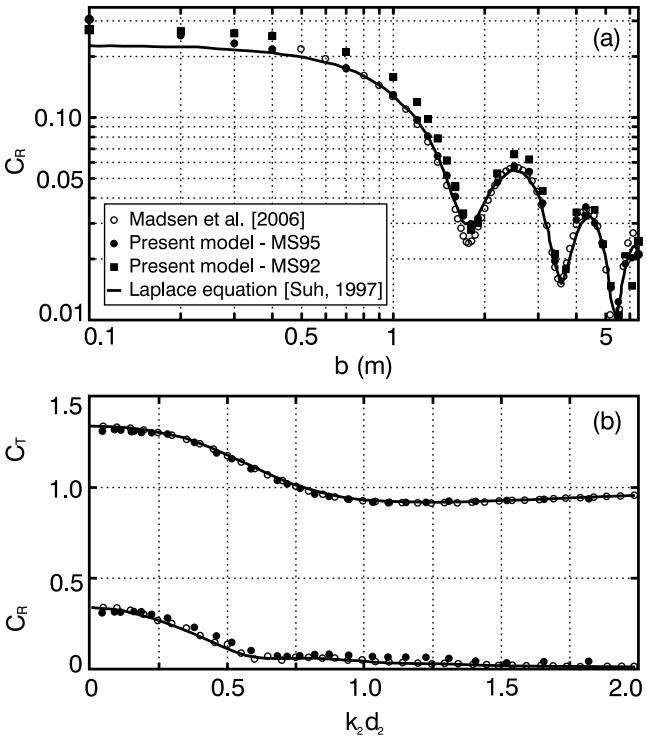

Figure 3. Plane shelf test cases: (a) reflection coefficient for fixed *kd* values and different slope widths; (b) reflection and transmission coefficients for a fixed bottom slope and different *kd* values.

and the numerical solution of *Madsen et al.* [1997]. The present solution underestimates the wave height near the breaking point due to the weak nonlinear properties of the governing equations. In fact, the same behavior can be seen in the results presented by *Madsen et al.* [1997]. Shortly after the onset of wave breaking, the wave height decreases and the agreement improves. As an additional validation of the ability of the scheme to capture the energy dissipation induced by wave breaking, the spatial evolution of the time-averaged energy flux has been computed and compared with the experimental one (Figure 2c). Initially the energy flux, as the wave height, is underestimated, but inside the surf zone the agreement is very good.

[30] The first test for a steep bottom slope was originally proposed by *Booji* [1983]. The topography consists of two horizontal bottom sections connected by a shelf of constant slope; the incoming water depth is 0.6 m and the final water depth is 0.2 m. The width of the plane shelf, b, is varied from 6.4 to 0.1 m, giving a range of bottom slopes between 1/16 and 4. The test is conducted using a monochromatic linear wave train with a period $T = 2.0$ s; the corresponding values of *kd* are 0.9 in the deep and 0.4 in the shallow sections. The grid size is $\Delta x = 0.02$ m and the time step $\Delta t = 0.005$ s. The simulations are performed first using the governing equations derived by *Madsen and Sørensen* [1992] under the assumption of mild bottom slopes and then their extension is applied to arbitrary bottom slopes [*Schäffer and Madsen*, 1995, hereafter SM95]. The results are presented in Figure 3a: the finite element solution of the Laplace equation [*Suh et al.*, 1997] is set as reference; the computed results are also compared with the solution of *Madsen et al.* [2006], who applied a set of fully nonlinear and highly dispersive Boussinesq-type equations for rapidly varying bathymetries. Such equations are, together with those proposed by *Lynett and Liu* [2004], the most accurate Boussinesq-type equations presented so far. The reflection coefficients computed using the equations in SM95 perfectly match the solution of *Madsen et al.* [2006] in the range $b = 6.4$–0.4, whereas a minor overestimation of wave reflection is shown when the equations from MS92 are applied. However, for bottom slopes higher than 1, the equations in MS92 give better results than their extension in SM95.

[31] The second case verifies the performances of the model in intermediate water. The bathymetry consists of a steep plane shelf of slope 0.5 connecting two regions of constant depth $d_1 = 20$ m and $d_2 = 5$ m. Monochromatic waves are generated in the deeper region; different wave periods have been considered, to cover a range of k_2d_2 values from 2 to 0.05 and of k_1d_1 from 8 to 0.1. The reflection and the transmission coefficients are plotted in Figure 3b; the present computations are compared with the reference solution of *Bender and Dean* [2003] and the calculations of *Madsen et al.* [2006]. The computed transmission coefficient agrees very well with the reference solution in the whole range of water depths. The agreement of the reflection coefficient is good in shallow waters but gets worse with increasing water depth.

[32] The previous cases, although dealing with steep slopes, consider shelves of finite length, therefore the accuracy of the results also depends on the representation of wave shoaling over the shelf. In these conditions, the solution is strongly affected by the presence of the slope. In the case of a vertical step, where there is no propagation over a steep slope but a discontinuity in the flux, the bottom slope has a reduced effect on wave dynamics.

[33] A last case concerning the propagation of solitary waves over an infinite step is now presented. The numerical domain is sketched in Figure 4a. The water depth in the deep section is $d = 1$ m and the wave height of the incident solitary wave is $H = 0.1$ m. The height B of the step is varied from 0.1 to 1.2 m. At the beginning of the computation, a rightward moving solitary wave is placed within the first 50 m of the domain; the simulation time is set to zero when the solitary wave crest reaches the position $x = 0$ m. The grid size is $\Delta x = 0.02$ m and the time step is $\Delta t = 0.0025$ s. The computed reflection and transmission coefficients are plotted in Figures 4b and 4c; the present numerical results are compared with the analytical solution calculated by *Lamb* [1932] using the linear long wave approximation. The reflection coefficient agrees very well with the theoretical solution by *Lamb* [1932] for low values of the ratio B/d; for ratios higher than 0.9, the Lamb's reflection coefficient is constantly greater than the numerical one. This is because, under the linear approximation, the reflection coefficient is predicted to become 1 when $B/d = 1$, whereas total reflection actually occurs when $B/d = 1 + 2H/d$ and no overtopping takes place. The calculated transmission coefficient closely follows the analytical solution of *Lamb* [1932] in the range 0.1–0.75; for B/d values higher than 0.8, the numerical transmission coefficient is significantly lower than the ana-

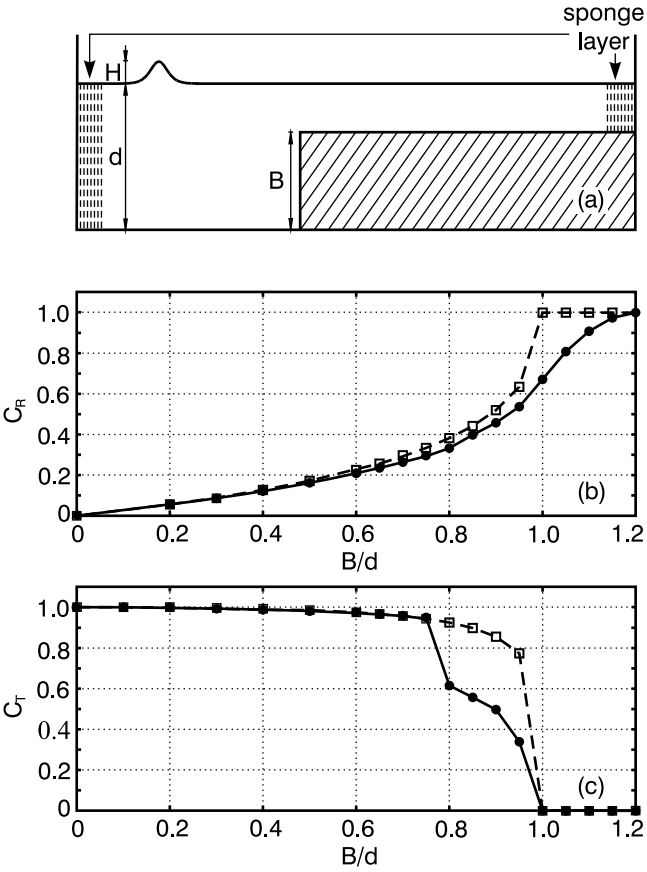

Figure 4. (a) Sketch of the numerical domain for the solitary wave test case, (b) reflection coefficient, and (c) transmission coefficient. Filled circles, present numerical results; squares, analytical solution by *Lamb* [1932].

lytical one because waves break over the shelf and energy is dissipated.

[34] On the basis of the previous test cases, the numerical model proves to be well equipped for the present application; a validation using field data would be useful to complete the assessment of the model's behavior but it is not yet available. Further studies are currently being performed in this direction.

2.2. Thrust Evaluation

[35] The outputs of the numerical model (time series of water depth and vertically averaged velocity) are used to evaluate the dynamical thrust exerted by waves on marsh boundaries. The computation is performed using the integral formulation of momentum conservation, which, for a control volume fixed in time and space, can be expressed as:

$$\int_{VC} \frac{\partial \rho \mathbf{v}}{\partial t} dV - \int_{SC} \rho \mathbf{v}(\mathbf{v} \cdot \mathbf{n}) dA = \int_{SC} \mathbf{T}^{(n)} dA + \int_{VC} \rho \mathbf{f} dV \quad (6)$$

where *VC* is a control volume, *SC* is the surface bounding the control volume, **v** is the velocity vector, **n** is the inward normal unit vector to the surface *SC*, $\mathbf{T}^{(n)}$ represents the

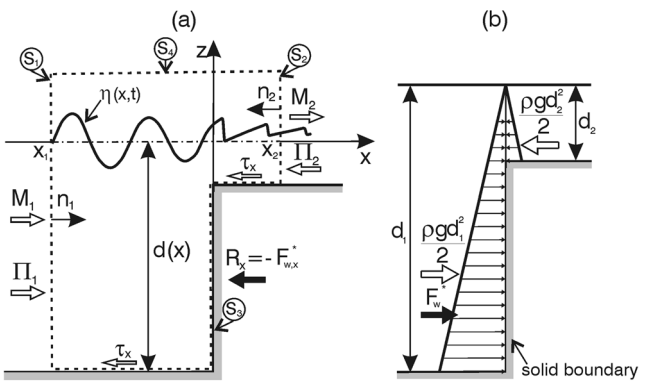

Figure 5. Sketch of (a) a standard control volume for thrust evaluation at a marsh boundary and (b) the relation between total and hydrostatic thrust at the wall.

surface forces per unit area, and **f** indicates the body forces per unit volume. The first term represents the instantaneous rate of momentum variation inside the control volume, the second is the momentum flux across the volume surface, and the two terms on the right-hand side of the equation are, respectively, the net surface and body force acting on the control volume (in this study, **f** is given only by the gravitational force).

[36] In the following, 2-D vertical cases of free surface, incompressible flows will be considered: a standard control volume is sketched in Figure 5a; the width of the control volume is assumed to be equal to 1 m and all the terms involved are given per unit width. The contribution of the air layer to the momentum balance is assumed to be negligible, thus the terms of the momentum equation are only specified for the water portion of the volume.

[37] For the purposes of the present study, we are interested in evaluating the resultant of the hydrostatic and dynamic pressure distributions acting on the boundary, therefore the wave thrust is always oriented normally to the surface of the marsh boundary. Since we consider simplified boundary geometries (Figure 6), for ease of calculation, we first evaluate the horizontal component of the wave thrust using only the projection along x of equation (6), and then we derive the normal thrust from its horizontal component.

[38] Considering that there is no momentum flux across the upper side of the control volume and across the bottom,

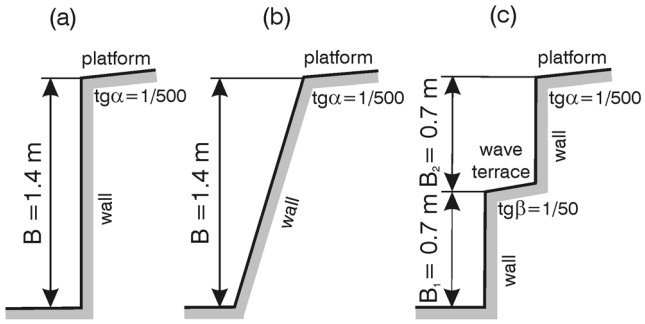

Figure 6. Standardized scarp configurations: (a) vertical bank, (b) sloping bank, and (c) terraced bank.

which is treated as impermeable, momentum conservation along x can be written as:

$$\rho \int_V \frac{\partial u}{\partial t} dV - \rho \int_{S_1} u^2 n_1 dA - \rho \int_{S_2} u^2 n_2 dA = \int_{S_1} p n_1 dA + \int_{S_2} p n_2 dA - \int_{S_3} \tau_x dA - R_x \quad (7)$$

where $n_1 = 1$ and $n_2 = -1$ are the inward normal directions to the control surfaces $S_1$and S_2, u is the velocity in the wave propagation direction, p is the pressure, τ_x is the bottom stress along x, and R_x is the horizontal reaction exerted by the wall on the control volume and it is equal to the horizontal wave thrust but oriented in the opposite direction.

[39] After application of the Leibniz theorem, the first term of equation (7) becomes:

$$I = \int_V \frac{\partial \rho u}{\partial t} dV = \rho \int_{x_1}^{x_2} \int_{-d}^{\eta} \frac{\partial u}{\partial t} dz dx = \rho \int_{x_1}^{x_2} \left[\int_{-d}^{\eta} u dz - u(\eta) \frac{\partial \eta}{\partial t} \right] dx = \rho \int_{x_1}^{x_2} \left[P - u(\eta) \frac{\partial \eta}{\partial t} \right] dx \quad (8)$$

P and η are given by the wave model, while the surface velocity $u(\eta)$ is reconstructed from the mean velocity value ($U = P/h$), considering the vertical distribution of horizontal velocity assumed in the Boussinesq approximation. Consistent with the order of the governing equations, the momentum flux M_i is expressed as:

$$M_i = \rho \int_{S_i} u^2 n_i dA = \rho \int_{-d}^{\eta} u^2 n_i dz = \rho \frac{P^2}{h} n_i; \; i = 1, 2 \quad (9)$$

where further terms deriving from the hyperbolic distribution of u along z have been neglected, being of higher order; the pressure force Π_i is given by:

$$\Pi_i = \int_{S_i} p n_i dA = \int_{-d}^{\eta} p n_i dz = \Pi_i^{hyd} + \Pi_i^{disp} = \rho \frac{g h^2}{2} n_i - \rho \left[\left(B + \frac{1}{3} \right) d^2 P_{xt} + \frac{d d_x}{6} P_t + g B d^2 (d_x \eta_x + d \eta_{xx}) \right]_i n_i; \; i = 1, 2; \quad (10)$$

both the hydrostatic and the dispersive contributions are kept where the Boussinesq approximation holds and only the hydrostatic contribution where the NSWE approximation is used.

[40] The integration of the bottom stress can be neglected in thrust evaluation due to the small dimension of the control volume adopted in the study. The total horizontal thrust per unit width on the wall is therefore calculated as:

$$F_{wx}^* = -I + M_1 + M_2 + \Pi_1 + \Pi_2 \quad (11)$$

having introduced equations (8) to (11) into equation (7) and being $F_{wx}^* = -R_x$ the magnitude of the horizontal thrust, positive when oriented toward the wall. The thrust due to wave action is evaluated from this thrust by subtracting the hydrostatic pressure acting on the wall when the water surface is at rest (Figure 5b):

$$F_{wx} = F_{wx}^* - \left(\rho g \frac{d_1^2}{2} - \rho g \frac{d_2^2}{2} \right) \quad (12)$$

If we approximate the surface of the marsh boundary with a plane, as will be the case in the tests presented in this work (Figure 6), the normal thrust can be computed from its horizontal component:

$$F_w = F_{wx} / \sin \theta \quad (13)$$

where θ is the angle formed by the surface plane with the horizontal direction x.

3. Study Site

[41] To determine the input parameters for our numerical model, we have surveyed the marsh edge geometry at the VCR, on the Atlantic side of the Delmarva Peninsula (Figure 7). The VCR shares the typical features of the shallow coastal barrier ecosystem bordering much of the Atlantic and Gulf coasts of the United States. It includes several barrier islands and shallow lagoons with extensive mudflats, fringed by *Spartina alterniflora* marshes both on the barrier island and on the mainland side. These marshes are dissected by a system of tidal creeks connected with subtidal flats and with a few intertidal relic oyster reefs. The lagoon is particularly shallow: water depths are below 1–2 m at mean low water (MLW), and approximately 50% of the lagoon surface area experiences water depths below 1 m at MLW [*Oertel*, 2001]. The shallow depths make the sediment susceptible to current and wave suspension [*Lawson et al.*, 2007]. Tides are semidiurnal and the mean tidal range is 1.2–1.5 m; high and low water levels can be modified during storm surges, depending on wind intensity and direction. Given the small tidal range and the weak tidal currents, storms are the primary agent of disturbance in the short term. Wind waves are the main cause of salt marsh deterioration through scarp erosion.

[42] Two different marsh boundary configurations have been mapped: at the south transect (Figure 7b), a cliffed edge characterized by a vertical scarp (Figure 7c) is present; at the north transect, there is a terraced bank (Figure 7d), compound of a lower and a higher scarp, separated by a short-wave terrace. The tip of the cliffed edge has an elevation of about 0.15 m above the mean sea level (MSL) and a total height of 1.5 m from the tidal flat; the angle at the base of the scarp is 79°. The highest platform of the terraced boundary lies around 0.15 m above the mean sea level, whereas the wave terrace starts at an elevation of −0.50 m with respect to the mean sea level. The overall height of the terraced edge is 1.4 m. The higher scarp, connecting the wave terrace and the marsh platform, has a slope angle of 80°, while the lower scarp inclination is 75°. The wave terrace has a mild slope of about 1/50 and it is 6 m long.

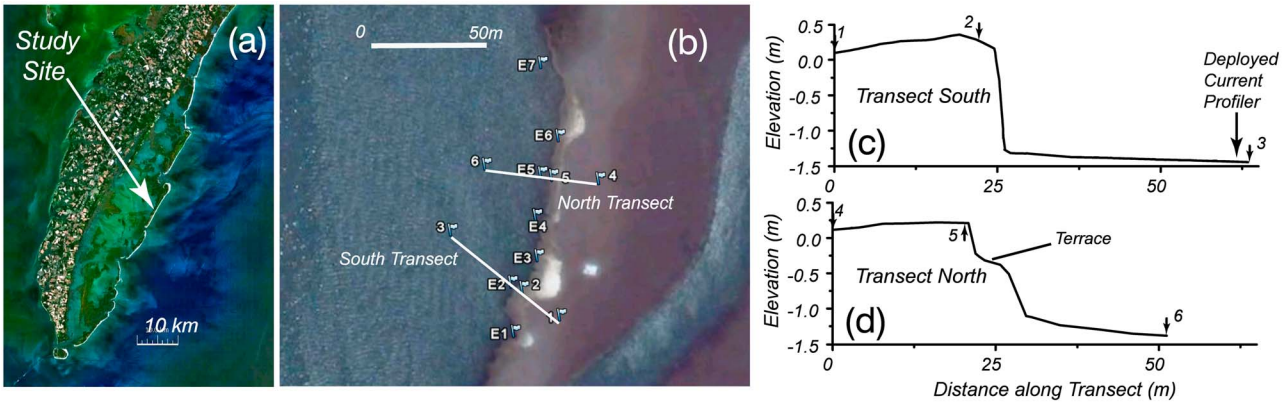

Figure 7. (a) Location of study site in the Virginia Coast Reserve (courtesy of NASA World Wind). (b) Location of surveyed transects in the back-barrier marshes of Hog Island (Google Earth imagery (c) Google Inc. Used with permission.). (c) South transect with vertical scarp; (d) north transect with wave terrace.

[43] To characterize the wave climate in front of the marsh scarp we deployed a Nortek Aquadopp current profiler at the south transect (Figure 7c) from 6 May 2008 to 7 April 2008. The current profiler recorded water elevations at 2 Hz every 30 min. Analysis of the wave data shows that during storms (wind speed >10 m/s) with wind blowing from north the root mean square wave height is H_{rms} = 0.20 m, the significant wave height is H_S = 0.30 m, $H_{1/10}$ = 0.40 m, and the peak period is T_P = 2 s.

4. Results

[44] This section presents the evaluation of the most critical conditions for marsh shoreline erosion as a function of wave climate and tidal elevation. In order to generalize the problem, three standard boundary configurations have been considered: a straight vertical bank (cliffed edge), a sloping scarp (ramped edge) with a constant slope of 0.7, and a terraced bank (Figure 6). The dimensional features of the first and third configurations have been extrapolated from the topography measured along the transects at the Virginia Coast Reserve site. The cliffed edge reproduces the south transect (Figure 7c) and the terraced bank reproduces the north transect (Figure 7d); the heights of the scarps at the two transects are slightly different, but for the standardized bathymetries, the same height of 1.4 m has been assumed. This is not expected to affect the response of the vertical scarp to wave attack since the governing parameter is the location of the marsh platform with respect to the mean water level position rather than the height of the scarp. The second test case has been added to investigate the differences in the response to wave action of a vertical and a sloping scarp.

[45] For all test cases, regular wave trains have been considered; wave periods and wave heights have been chosen according to a statistical analysis of the data collected in a measurement campaign at the aforementioned site (see previous section). In order to evaluate the variation with tidal elevation of the hydrodynamic action held responsible for the erosive phenomenon, several simulations with different tidal levels were performed; the MWL positions were set to conform to the recorded tidal range at the VCR site.

[46] The numerical domain is 170 m long and the toe of the bank is located 150 m downstream of the wavemaker boundary (left end of the domain). At the right end of the domain, an absorbing boundary condition is imposed to dissipate the energy arriving at the boundary when waves propagate over the platform. When waves swash on the scarp or overtop the bank but do not reach the right-hand boundary, the moving shoreline is automatically handled and no specific algorithm is required. The grid size is Δx = 0.025 m and the time step is Δt = 0.0025 s. For the vertical bank case, in the tests where no overtopping occurs, the scarp is simulated introducing a fully reflective condition; in all the other tests, the scarp is not perfectly vertical but it has a width of five cells, giving at the toe an angle of 85° instead of 90°, a difference that is considered negligible.

4.1. Vertical Bank

[47] In order to evaluate the response of a vertical scarp to wave action, a standardized configuration, consisting of a 1.4 m high bank followed by a platform of slope 1/500, was used. Ten different tidal elevations (d = 0.9; 1.0; 1.1; 1.2; 1.3; 1.5; 1.6; 1.8; 2.1 m), both above and below the bank height, were considered.

[48] The first series of tests have been conducted using a wave period T = 2.0 s, corresponding to the peak wave period given by the measurements, and a wave height H = 0.30 m, which is the measured significant wave height. Figure 8 shows the envelopes, over two periods, of the water surface elevation close to the bank. For tidal elevations lower than 1.2 m, the waves do not overtop the bank and are fully reflected by the vertical scarp; the wave height at the edge doubles the incident wave height. At the tidal levels d = 1.2 m (not shown in Figure 8) and d = 1.3 m, the maximum water surface elevation at the scarp determines the overtopping of the bank: a thin layer of water rushes up and down the flat portion of the bank following the wave cycle. When the tidal elevation is above 1.4 m, the bank is completely submerged and the wave height at the scarp is lower than in the previous cases. Wave propagation is affected by the water depth on the flat portion of the bank: at

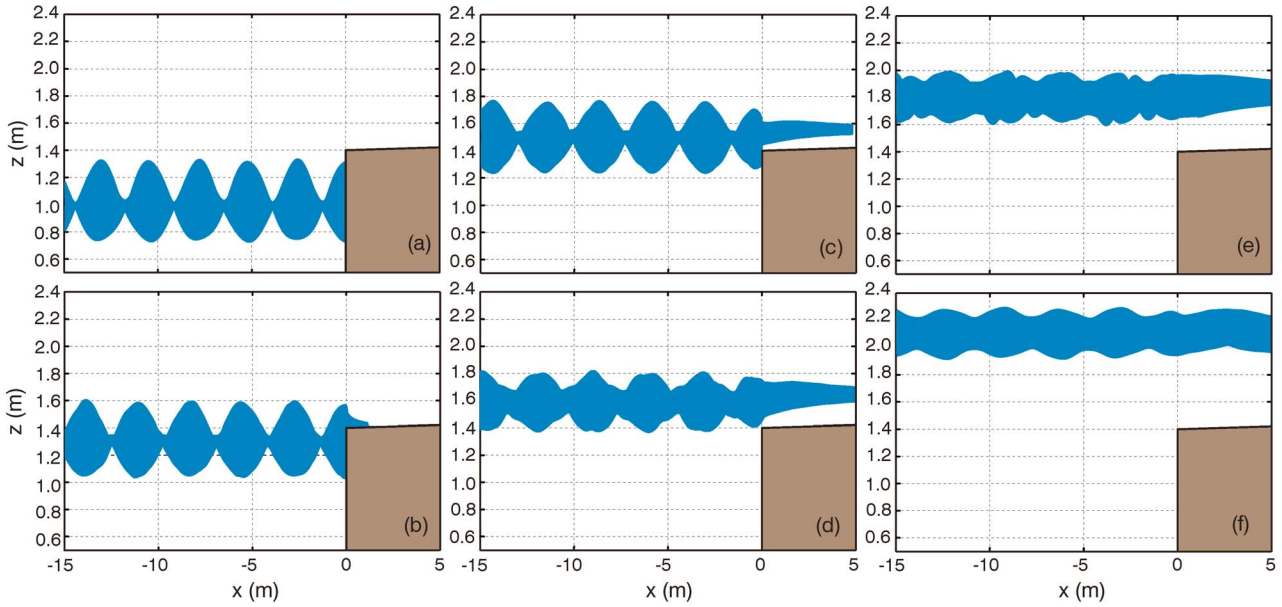

Figure 8. Water surface elevation envelope for the vertical bank case: (a) $d = 1.0$ m; (b) $d = 1.3$ m; (c) $d = 1.5$ m; (d) $d = 1.6$ m; (e) $d = 1.8$ m; (f) $d = 2.1$ m.

tidal elevations d = 1.5, 1.6, and 1.8 m, waves break immediately after surpassing the scarp and the effect of reflection on the wave height is still relevant, while, at higher tidal elevations (e.g., d = 2.1 m in Figure 8), the influence of the bank on wave propagation is reduced. Figure 9a presents the variation of the relative wave height at the edge of the bank (x = 0 m).

[49] Energy reflection, transmission, and dissipation at the scarp can be evaluated from wave height data. An energy balance equation is solved for a control volume fixed across the scarp, and the model outputs are then used to evaluate wave height and mean water level position. Finally, linear theory is applied to compute the incoming, reflected, and transmitted energy fluxes and hence determine the amount of energy dissipation inside the control volume. The ratio of time-averaged energy dissipation over incoming wave energy flux is plotted in Figure 10a; there is no dissipation for the lowest tidal elevations where energy is completely reflected at the scarp or for the highest elevation where waves propagate over the bank without breaking (although the effect of marsh vegetation on wave attenuation is not accounted for in this analysis). Energy dissipation takes place when waves slam against the bank edge and overtop it and when the water depth over the platform is low enough for waves to break over it.

[50] The time-varying normal thrust exerted by the waves on the bank has been computed for each test case; Figure 11a shows the difference between the maximum thrust and the minimum thrust (respectively higher and lower than the hydrostatic force due to the MWL) at different tidal elevations; the variation of the maximum thrust is plotted in Figure 11b. Because of some scattering in the results, especially for the cases involving the overtopping and rundown on the scarp, which were the most difficult to simulate numerically, best-fitting curves have been drawn following the numerical solution. The thrust initially increases with tidal elevation until the depth d = 1.2 m is reached and waves start to overtop the bank, and then the thrust keeps approximately constant for mean water levels between 1.2 and 1.5 m. At values of d > 1.5 m, the thrust decreases rapidly with increasing tidal level, eventually tending to a constant condition when the tidal elevation is so high that there is no interaction between the bank and the waves. Figure 11c presents the maximum stress acting on the bank at different tidal elevations, computed by dividing the maximum thrust $F_{w,\max}$ by the area of the part of the wall that has been wetted by waves.

[51] Two more series of test cases have been performed using the same bank configuration in order to investigate the effect of wave height on wave thrust. A wave period of 2.0 s and wave heights H = 0.20 m (the maximum H_{rms} measured in the field) and H = 0.40 m (the maximum measured $H_{1/10}$) have been chosen. The results are plotted in Figure 12.

[52] At a given tidal elevation, the thrust exerted by the wave trains on the bank edge increases with the height of the incoming waves. In all cases, the maximum thrust is reached at tidal elevations where the wave crests get to the top of the bank, without occurrence of significant overtopping.

4.2. Sloping Bank

[53] The sloping bank (Figure 6b) consists of a 1.4 m high plane with a constant slope of 0.7. To allow a comparison with the vertical bank results, the same tidal elevations and wave train parameters (T = 2.0 s and H = 0.30 m) of the previous case were adopted. Figure 13 shows the envelopes of the water surface elevation close to the bank.

[54] The overall behavior is similar to the one observed for the propagation of waves on the vertical bank. The most relevant difference is the development of a wide runup-rundown motion along the slope. Because the tongue of water rushes up and down fast, the runup tip climbs high on the slope and overtopping starts earlier than in the vertical case. The maximum wave height immediately before the scarp is reduced compared to the previous case because of

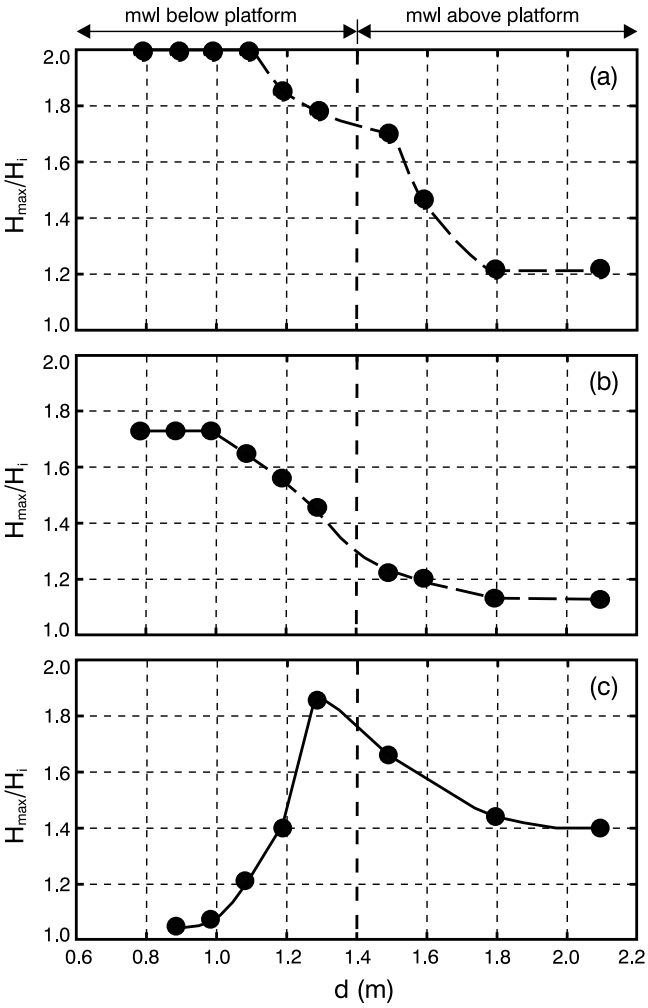

Figure 9. Evolution with tidal elevation of the maximum wave height at the edge of the scarp for a (a) vertical bank (x = 0 m); (b) sloping bank (x = –0.86 m); and (c) terraced bank (x = 6.45 m).

the lower reflection and the earlier occurrence of overtopping (Figure 9b).

[55] The wave thrust and stress are plotted in Figure 14. The evolution of the thrust with tidal elevation resembles that of the vertical case, with a thrust first increasing with tidal elevation, getting to its maximum value when waves reach the top of the scarp, and then decreasing when the bank is completely submerged. The maximum thrust values are significantly higher than in the previous case, but this can be explained by the bigger extent of the scarp, which is much longer. In fact, the values of the normal stress are slightly higher but comparable to those exerted on the vertical scarp. As in the previous case, wave height data are used to evaluate the energy dissipation occurring at the scarp (Figure 10b). Energy dissipation is maximum for tidal elevations close to the platform level.

4.3. Terraced Bank

[56] The last bathymetry reproduces a simplified terraced bank compound of two 0.7 m high steps; the terrace is 2 m long and has a slope of 1/50 (Figure 6c). As in the previous test cases, regular wave trains with period T = 2.0 s and H = 0.30 m were used and eight different tidal elevations, ranging between 0.90 and 2.1 m were considered. The water surface envelopes are plotted in Figure 15.

[57] Figure 16 shows the evolution of the thrust and stress exerted by waves on the bottom step and on the top step of the terraced scarp. The evolution of the maximum wave thrust (Figures 16a and 16b) and the difference between maximum and minimum thrust (Figures 16c and 16d) are similar. On the bottom step, high forces are exerted both at tidal levels close to the elevation of the terrace when the waves splash against the step and break at its corner and at levels around the height of the second platform when overtopping occurs. The top part of the scarp is subject to small wave thrusts at low tidal elevations (d < 1.3 m) because breaking occurs at the edge of and over the first platform and the height of waves reaching the higher section of the scarp is significantly reduced (Figure 9c). The magnitude of the wave thrust increases at tidal levels close to the elevation of the second platform when water depth over the terrace is high enough for waves not to break. The maxi-

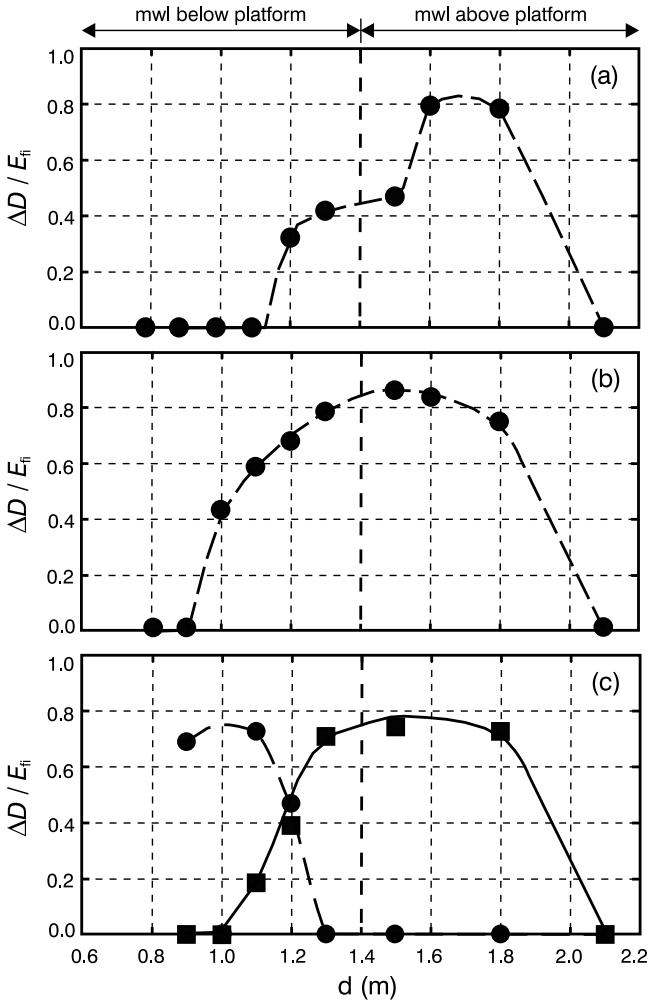

Figure 10. Evolution with tidal elevation of wave energy dissipation across the scarp for a (a) vertical bank, (b) sloping bank, and (c) terraced bank. Circles, bottom scarp and wave terrace; squares, top scarp and platform.

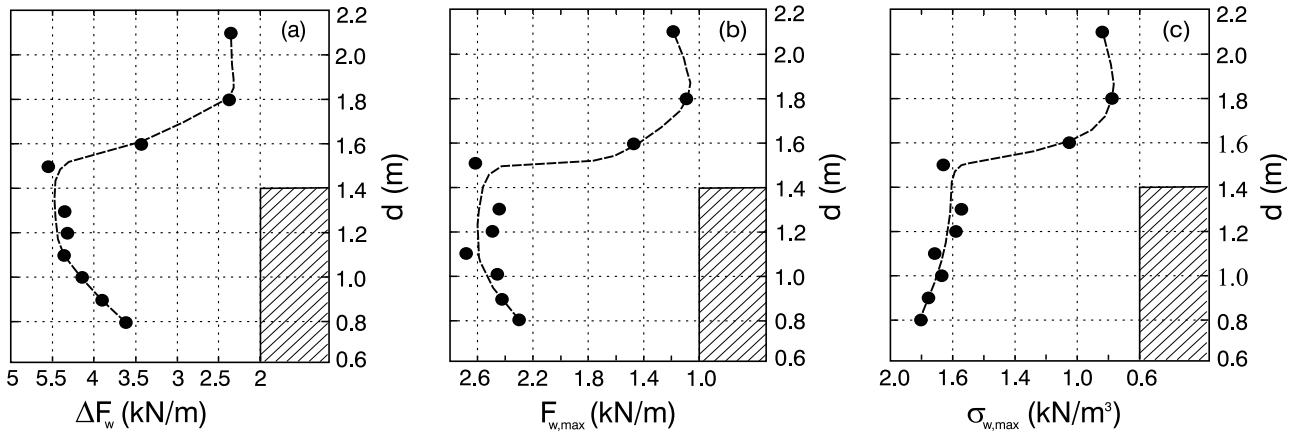

Figure 11. Wave thrust evolution at different tidal elevations for the vertical bank case: (a) difference between maximum and minimum wave thrust, (b) maximum wave thrust, and (c) maximum stress.

mum normal stress exerted on the lower scarp (Figure 16e) experiences little variation with tidal level and it is relatively small, whereas the stress on the top scarp (Figure 16f) is very small for low tidal elevations but attains quite high values when the MWL is close to the elevation of the second platform.

[58] The outputs of the model are used to compute the energy reflection, transmission, and dissipation occurring as waves propagate against and over the bank. Results are given in Figure 10c. The energy dissipation taking place at the bottom scarp and over the wave terrace has been separated from the energy dissipation occurring at the top scarp and over the platform. At tidal elevations $d \leq 1.2$ m, waves slam against the low step, losing part of their energy, and then breaking occurs over the terrace and, as waves move forward, most of the incoming energy is dissipated in turbulence generation before the top wall is reached, as confirmed by the small values of the thrust exerted on the upper scarp (Figure 16d). As tidal level grows, the repartition of energy dissipation between the low and the high step (Figure 10c) shows that the influence of the first step on wave propagation progressively decreases and most of the dissipation takes place at the upper wall and over the platform. The maximum energy dissipation at the top scarp and over the platform is reached at mean water level values between $d = 1.3$ m and $d = 1.5$ m, when all energy dissipation happens across the second scarp and it is due to waves crushing against and overtopping the high step or breaking over the platform. The overall energy dissipation is stronger at tidal elevations close to the mean water level.

[59] Figure 17 compares the wave thrust acting on the vertical ($F_{w,ver}$) and on the terraced ($F_{w,ter}$) bank for a given wave train and set of tidal elevations: the modulus of the difference between the maximum and minimum total thrusts ($|F_{w,ver}| - |F_{w,ter}|$) in the two cases are given, respectively, in Figures 17a and 17b. The difference tends to zero for very high tidal elevations, as the bank shape exerts less of an influence on wave propagation. At lower values of water level, both the maximum and minimum thrust exerted on the vertical edge are bigger in absolute terms. Such behavior is due to the fact that for the terraced bank, at low tidal elevations, waves get attenuated traveling over the lower platform. Therefore, the maximum thrust and the amplitude of thrust variation over a wave period ($F_{w,\max} - F_{w,\min}$) are reduced.

5. Discussion

[60] The outputs of the numerical simulations have been used to evaluate the wave thrust and the energy dissipation

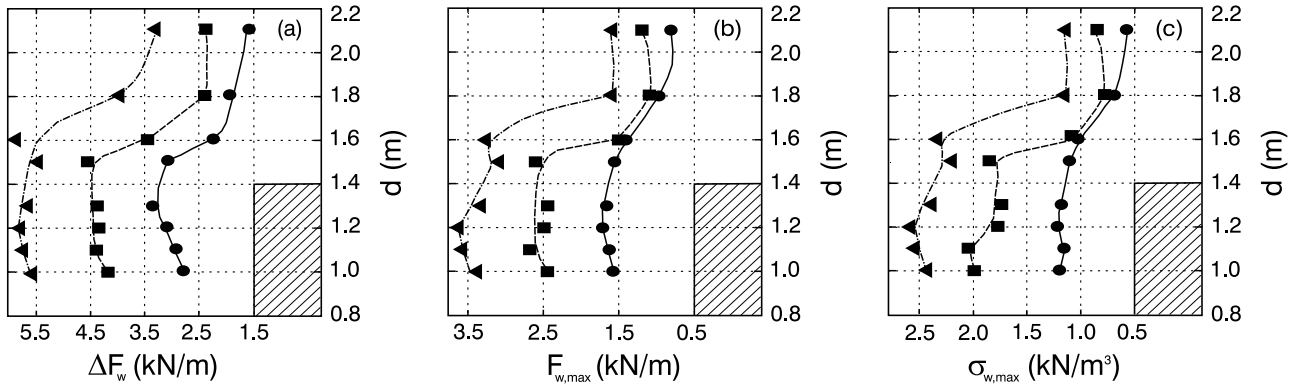

Figure 12. Wave thrust variation with tidal elevation and wave height. Triangles, $H = 0.40$ m; squares, $H = 0.30$ m; circles, $H = 0.20$ m. (a) Difference between maximum and minimum wave thrust. (b) Maximum wave thrust. (c) Maximum stress.

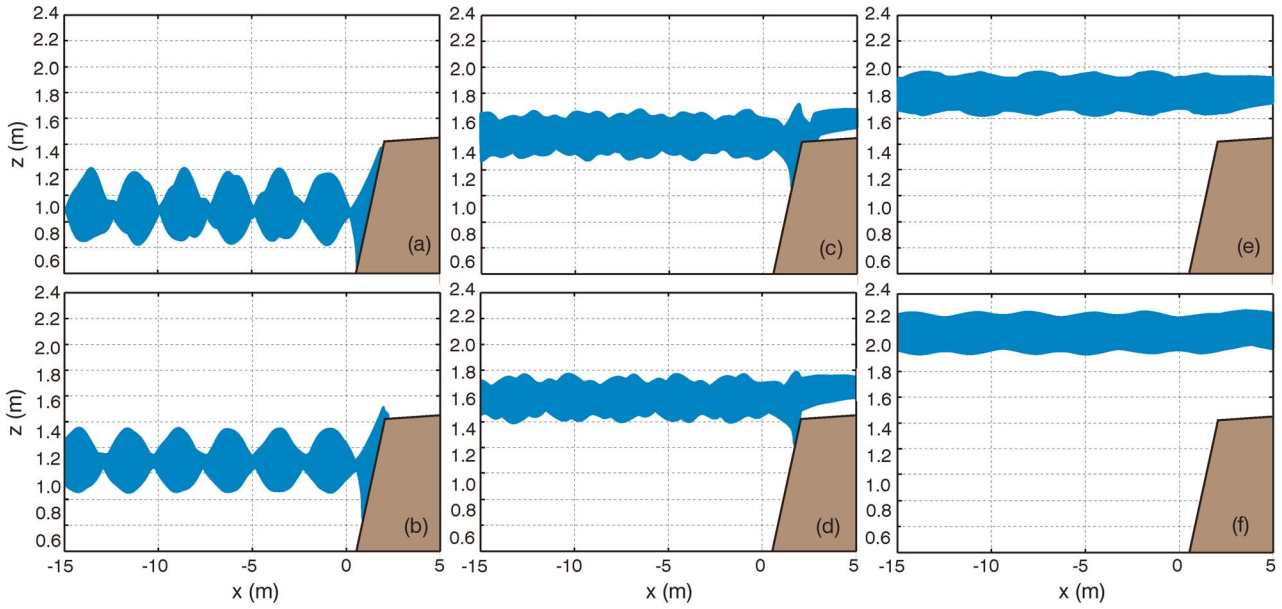

Figure 13. Water surface elevation envelope for the sloping bank case: (a) $d = 1.0$ m; (b) $d = 1.1$ m; (c) $d = 1.5$ m; (d) $d = 1.6$ m; (e) $d = 1.8$ m; (f) $d = 2.1$ m.

occurring as waves interact with a marsh boundary. The wave thrust is held responsible for the detachment of entire mud blocks from the marsh edge; the higher the maximum thrust ($F_{w,\max}$) and maximum stress ($\sigma_{w,\max}$), the more likely block removal. Also, because during a wave cycle the thrust is higher than the hydrostatic loading for half of a wave period and lower for the remaining half, the amplitude of the wave thrust (ΔF_w) can be considered an indicator of the exposure of the marsh edge to wetting and drying, which is one of the phenomena responsible for the weakening of the bank material. Energy dissipation is a consequence of wave breaking. Therefore, the related erosional mechanism is expected to be scour, driven by turbulence and bottom shear stresses.

[61] The analysis of the numerical results indicates that wave action on marsh edges is strongly related to tidal level. For all the examined bathymetries, the highest values of maximum thrust and thrust amplitude are reached when the mean water level (d) is close to the platform elevation (B); being that $B = 1.4$ m in the simulations, the strongest forces are exerted when d is within the range 1.2–1.5 m. The basin at the study site is microtidal; consequently, the marsh platform is close to MSL and, although subject to storm surges and meteorological low tides, the range of water elevations associated with the highest thrusts is the most frequent during the tidal cycle. Therefore, in microtidal environments, salt marshes are in a critical range of elevations that maximizes boundary erosion.

[62] The evolution of wave energy dissipation with tidal level is different for the three edge configurations: for the vertical and sloping bank test cases, the maximum dissipation takes place when waves submerge the platform, which occurs when $d = 1.6$–1.8 m at the vertical edge and $d = 1.3$–1.5 m at the sloping edge, because the swash motion enhances wave propagation over the platform. For the terraced edge, the overall energy loss is high at all tidal elevations

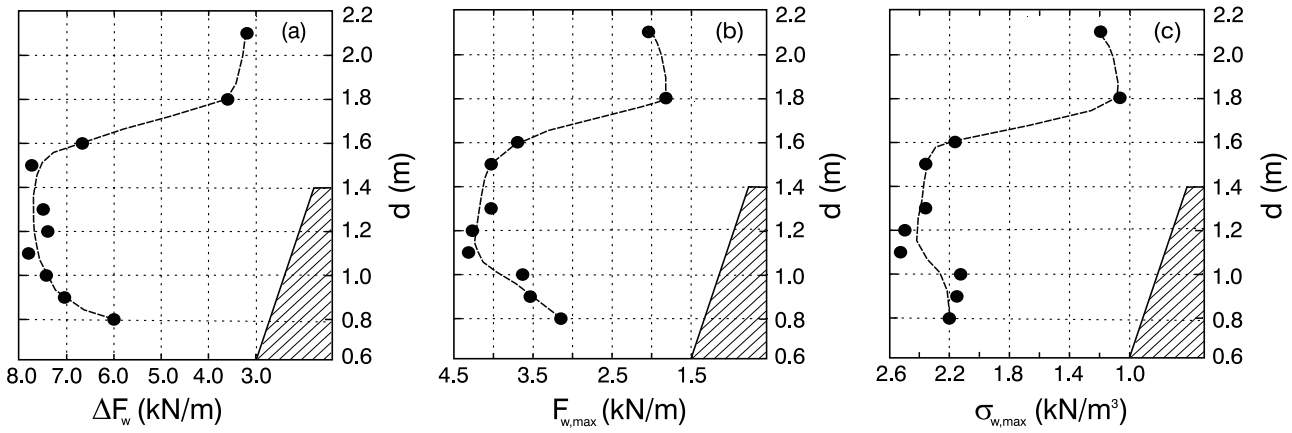

Figure 14. Wave thrust evolution at different tidal elevations for the sloping bank case: (a) difference between maximum and minimum wave thrust, (b) maximum wave thrust, and (c) maximum stress.

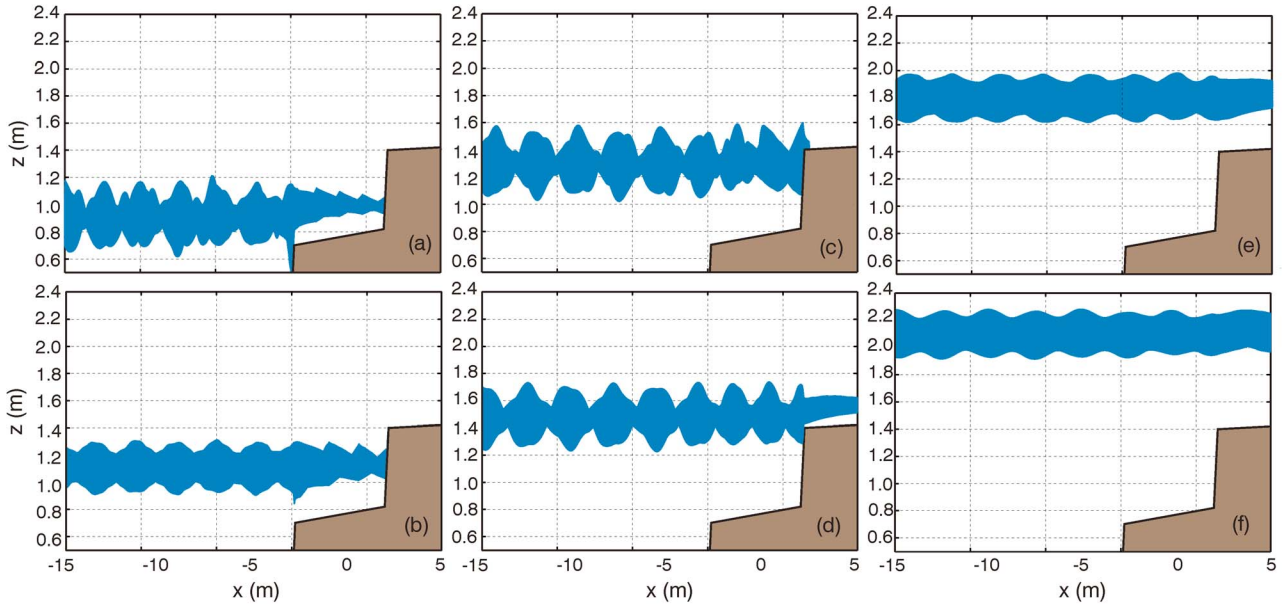

Figure 15. Water surface elevation envelope for the terraced bank case: (a) d = 0.9 m; (b) d = 1.1 m; (c) d = 1.3 m; (d) d = 1.5 m; (e) d = 1.8 m; (f) d = 2.1 m.

around the mean water level; the repartition of energy dissipation between the two scarps shows that, as the mean water level increases, the location of energy dissipation moves from the terrace to the top scarp. At high tidal elevations, when the marsh is submerged, energy dissipation is expected to affect platform erosion more than terrace and scarp erosion. For all test cases, the maximum values of energy dissipation are reached for water depths within the regular tidal range at the study site.

[63] According to the results of our study, the worst conditions of wave thrust and energy dissipation occur when the tidal level is close to, or immediately above, the platform elevation. Low marshes, because of their position with respect to the tidal range and the fact that the water level is more frequently at their elevation during the tidal cycle, are the most exposed to wave attack and they are expected to experience block detachment (particularly in situations with vertical and sloping banks) as well as sediment erosion at the marsh tip or on the wave terrace, when present. For marshes higher in the tidal range, the water level is seldom at the marsh elevation; consequently, the main erosional agent is not the thrust exerted by waves, but bottom shear stresses. The most frequent feature of marsh deterioration is thus expected to be scarp undercut rather than block removal.

[64] As the salt marsh matures, the elevation of the high marsh increases and the mean water level reaches the platform elevation less frequently. Therefore, wave thrust becomes less significant and block erosion seldom takes place. Therefore, edge erosion should be maximum for young marshes in the first stages of the accreting process or for drowning marshes (i.e., marshes that cannot keep pace with sea level rise).

[65] Vertical and sloping banks are the worst geometry for wave thrust: waves exert high stresses on the marsh edge. The terraced bank is the least exposed to wave thrust, especially at its bottom portion. Nevertheless, this last configuration is exposed to the occurrence of wave breaking over the terrace and at the top scarp. In such conditions, the leading erosion mechanism is probably related not to the pulse transmitted by waves hitting the scarp, but to the scour caused by breaking generated turbulence. Therefore, the terrace and the top scarp are likely to experience bottom stress erosion, scour, and undercut more than block detachment. In time, the terrace is eroded and the vertical scarp geometry recovered. However, until then, we expect a lower rate of boundary erosion.

[66] As already discussed, the maximum value of wave thrust is reached when wave crests lap the top of the marsh scarp and remains about constant with increasing tidal elevation until the marsh is fully submerged, then, at high tidal elevations, the wave thrust decreases. Energy dissipation, too, is maximum when the tidal elevation is around the platform or the terrace level. Energy dissipation is evidence of wave breaking occurrence and the associated erosion is primed by turbulence and bottom shear stresses. For the first two configurations (vertical scarp and sloping scarp), this type of erosion mostly takes place over the platform while the scarp is more affected by wave thrust; at the terraced edge, the erosional mechanism induced by wave breaking is stronger than in the previous conditions and it is particularly relevant on the wave terrace and at the top scarp. On the vertical scarp, the peak thrust occurs before the peak energy dissipation during flood, whereas during ebb the opposite is true. In fact, the energy dissipation peaks at elevations between 1.6 and 1.8 m above the tidal flat elevation (Figure 10a), whereas the thrust peaks between 1.4 and 1.6 m (Figure 11b). If, as we expect, wave thrust is responsible for block detachment and energy dissipation is responsible for sediment erosion, then it is possible that storms occurring during ebb events are more effective in eroding the scarp, with the ebbing currents carrying offshore the sediments mobilized by turbulence and the wave impact detaching the blocks.

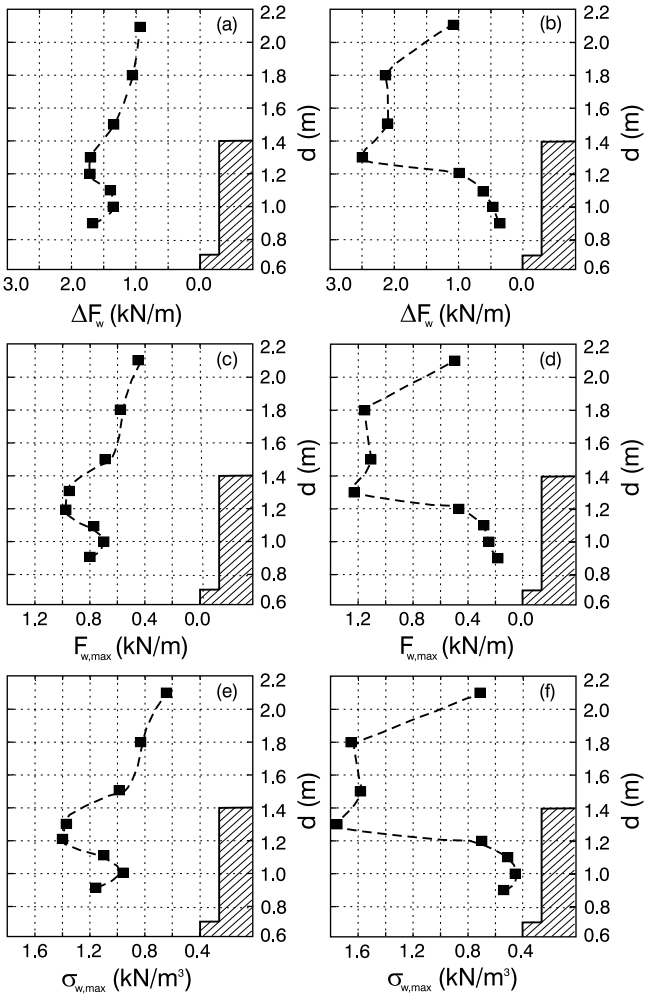

Figure 16. Wave thrust evolution at different tidal elevations for the terraced bank case: (a) difference between maximum and minimum wave thrust on the bottom step, (b) difference between maximum and minimum wave thrust on the top step, (c) maximum wave thrust on the bottom step, (d) maximum wave thrust on the top step, (e) maximum stress on the bottom step, and (f) maximum stress on the top step.

[67] In the proposed test cases, the wave train parameters were kept constant regardless of the simulated tidal level; this simplification was assumed in order to separate the effect of MWL elevation on the results. At the study site, which is a sheltered system of shallow lagoons, the waves reaching the marsh shores are generated locally within the tidal basin. Wave generation is affected by the elevation of the MWL in two ways: in shallow waters, the growth of wave height and wave period is limited by the interaction with the bottom due to frictional losses. Moreover, fetch extension increases with raising water depth because the extent of emergent land surface decreases [*Department of the Army, Waterways Experiment Station, Corps of Engineers, and Coastal Engineering Research Center*, 1984; *Fagherazzi and Wiberg*, 2009]. It can reasonably be expected that the generation of higher waves takes place when water in the basin is deeper; however, given the small tidal range at the study site, wave generation is also more sensitive to the presence or absence of storm surges than to predicted tidal elevation.

[68] The influence of a limited range of wave heights on wave thrust has been evaluated for the vertical test case (Figure 12). Considering wave heights, varying as a function of water depth, it can be highlighted that the worst conditions for marsh erosion occur when the MWL is around the platform level: wave thrust would be further reduced at low tidal elevations, while at high water depths, its decay with raising level is too fast to be compensated by the increase induced by higher wave heights. A slight enlargement of the range of water levels favoring high thrusts can be expected when wave height is treated as a function of water depth and hence modified together with the mean water level, instead of kept constant (which is the case of the present computations).

[69] Considering energy dissipation, having smaller wave heights at low water depths does not alter the behavior described in the previous sections, while the occurrence of bigger waves at high tidal levels would further enhance breaker formation over the platform, thus confirming that the platform, together with the wave terrace, are the most affected by turbulence erosion.

[70] It is important to note that the results presented herein are derived under two strong simplifying hypotheses: first, only two fixed friction coefficients are used, one for the tidal flat and one for the platform, whereas in salt marshes bottom friction depends on the characteristics of the vegetation cover and, hence, can change over short to medium time scales in response to storm events or seasonal variations (see, for instance, *Möller et al.* [1999] and *Möller and Spencer* [2002]). Moreover, the choice of the friction factor value, especially with regard to the platform and the wave terrace, is affected by a certain amount of uncertainty since it is very difficult to estimate surface friction from field parameters.

[71] The second simplification is considering only monochromatic waves impacting the marsh boundary perpendicularly. In salt marshes, waves with different periods will attack the scarp from different directions, further increasing the complexity of the processes at play. The action of the wave thrust on the marsh edge is an impulsive phenomenon and we expect high thrusts to be the most effective in causing block detachment. The intensity of the wave thrust, for a given water depth, is strongly related to the magnitude

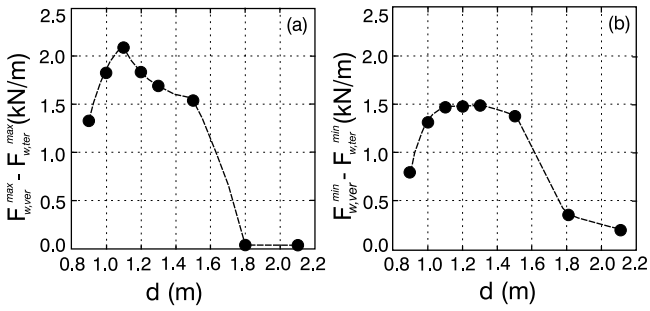

Figure 17. Comparison of (a) maximum and (b) minimum wave thrust for the vertical and terraced bank case.

of the wave height; therefore, if we consider a random sea state characterized by a significant wave height equal to the height of the simulated monochromatic wave train, we expect to find a number of higher waves (resulting in higher wave thrusts), which, however, will be less frequent than waves close to the significant height. It would be interesting to investigate whether marsh boundaries are eroded more efficiently by very high thrusts, even if isolated in time, or by frequent, repeated but smaller thrusts. This might be the object of further studies. In this work, we decided to use the significant wave height to consider a compromise condition. The effects of turbulence and bed shear stresses, here estimated through energy dissipation, are not governed by the presence of isolated, high waves but are driven by the overall intensity of the whole storm event, which can be described by the root-mean-square wave height H_{rms}. The root-mean-square wave height is representative of the energy content of an irregular wave field; therefore, if the monochromatic wave simulation is performed adopting the root-mean-square wave height and the energy wave period as wave parameters, we expect the results for the dissipation of energy at the marsh edge to reasonably represent the mean effect of the storm on the marsh margin. The significant wave height is slightly higher than the root-mean square wave height but it is still a good, precautionary representation of the energy content of an irregular wave field. In fact, it is normally used to evaluate the action of waves on structures.

[72] Wave energy impacting the marsh boundary is controlled by mudflat elevation [*Möller et al.*, 2009; *Mariotti and Fagherazzi*, 2010] and fetch distances [*Möller et al.*, 2009]. Here we focus on the last 15 m of tidal flat just in front of the marsh scarp, thus assuming an incoming wave that was generated and propagated elsewhere. The relationship between wave height and tidal elevation is strongly coupled to the distribution of landforms within the lagoons as well as to local wind climate [*Fagherazzi and Wiberg*, 2009]. For example, it is likely that the system switches from depth-limited conditions at low water, with bottom dissipation limiting wave height, to fetch-limited conditions at high tidal elevations or during storm surges. This threshold effect might increase the energy of impacting waves at high water, possibly augmenting erosion of the cliff top during high tides. The coupling of our model to the models of *Fagherazzi and Wiberg* [2009] and *Mariotti and Fagherazzi* [2010] or to the framework of *Möller et al.* [2009] could shed light on the effects of depth- and fetch-limited conditions on the erosion of salt marsh boundaries by wave attack.

[73] Finally, our model results can be coupled to geotechnical models for bank stability in order to determine the mechanisms responsible for scarp erosion of marsh boundaries. Our numerical simulations are in agreement with the field results of *Pringle* [1995] in Morecambe Bay, UK. Ten years of marsh erosion measurements showed that a combination of high tidal and wind-wave conditions were highly correlated to major peaks in the mean monthly marsh edge erosion. *Pringle* [1995] concluded that erosion occurred during flood before the salt marsh is immersed and at the beginning of the ebb phase when the water level is just below high water. It is also important to note that the scarp geometry presented herein (Figure 6) might not be representative of all marsh boundaries. A small tidal flat channel running parallel to the marsh edge is common in the marshes along the Danish Wadden Sea [*Pedersen and Bartholdy*, 2007]. Levees develop both between the tidal channel and the marsh cliff and on the seaward side of the channel. Such complex geometry might impact wave propagation and therefore the evolution of the marsh scarp.

6. Conclusions

[74] The following conclusions can be deduced by our model simulations:

[75] 1. For a vertical marsh scarp, incoming waves are fully reflected at tidal elevations below the marsh platform, producing a wave height double that of the incoming wave. For water levels above the marsh platform, the wave height at the scarp decreases since the waves are transmitted over the marsh platform and are not only reflected. For a sloping scarp, wave reflection is less pronounced and, again, the wave height decreases for water elevations above the marsh platform. In a terraced scarp, for intermediate tidal elevations (above the first terrace and below the platform), the waves are partly reflected by the wall and partly dissipated on the terrace; therefore, lower waves reach the top scarp. For tidal elevations close to the top scarp elevation, waves bypass the terrace and are reflected by the top scarp. For tidal elevations above the marsh, waves are transmitted on the marsh platform and then dissipated.

[76] 2. Wave thrust on the marsh scarp strongly depends on tidal elevation. On a vertical and sloping scarp and for a given wave height, the thrust increases with tidal elevation until the marsh is submerged, and then the thrust rapidly decreases. In a terraced scarp, the lower terrace absorbs most of the thrust as long as the tidal elevation is low enough for waves to break over the terrace surface, whereas the thrust on the top scarp is negligible. For elevations close to the marsh platform, both steps experience the highest thrust. For elevations above the marsh platform, the wave thrust rapidly decreases. The thrust is maximum for the vertical and sloping scarps and minimum for the terraced scarp.

[77] 3. At a vertical scarp and for a given wave height, wave energy dissipation is maximized just above the marsh platform elevation when wave reflection is reduced and wave breaking occurs at the marsh edge. At a sloping scarp, energy dissipation is maximized just below the marsh platform elevation since the swash motion on the sloping surface reduces wave reflection and promotes energy dissipation. At a terraced scarp, wave energy is dissipated on the terrace for lower tidal elevations, and then on the top scarp for elevations just around the marsh platform. The total energy dissipation remains constant for tidal elevations just around the marsh scarp, and then decreases when the marsh is inundated.

[78] 4. More research is needed to better quantify the impact of wind waves on marsh boundaries. Future work will verify the numerical results by field measurements of wave transformation across different edge morphologies, conduct a set of numerical model experiments that are better able to isolate the importance of wave spectra and direction, and determine the relative role played by the geotechnical properties of salt marsh substrates at these edge transitions (e.g., organic content, grain size, the "armoring" of cliffs through shell debris and vegetation mats).

[79] **Acknowledgments.** This research was supported by the U.S. Department of Energy's Office of Science (BER) through the Coastal Center of the National Institute for Climatic Change Research at Tulane University award TUL-538-06/07, NSF through the VCR-LTER program award GA10618-127104, and the Office of Naval Research award N00014-07-1-0664.

References

Allen, J. R. L. (1990), Salt-marsh growth and stratification: A numerical model with special reference to the Severn Estuary, southwest Britain, *Mar. Geol.*, *95*(2), 77–96.

Allen, J. R. L. (2000), Morphodynamics of Holocene saltmarshes: A review sketch from the Atlantic and Southern North Sea coasts of Europe, *Quat. Sci. Rev.*, *19*, 1151–1231.

Allen, J. R. L., and M. J. Duffy (1998), Medium-term sedimentation on high intertidal mudflats and salt marshes in the Severn Estuary, SW Britain: The role of wind and tide, *Mar. Geol.*, *150*(1–4), 1–27.

Brocchini, M., R. Bernetti, A. Mancinelli, and G. Albertini (2001), An efficient solver for nearshore flows based on the WAF method, *Coastal Eng.*, *43*, 105–129.

Barbier, E. B., et al. (2008), Coastal ecosystem-based management with nonlinear ecological functions and values, *Science*, *319*, 321–323, doi:10.1126/science.1150349.

Basco, D. R., and I. A. Svendsen (1984), Modeling turbulent bore propagation in the surfzone, in *Nineteenth Coastal Engineering Conference: Proceedings of the International Conference*, edited by B. L. Edge, pp. 99–114, Am. Soc. of Civ. Eng., New York.

Bender, C. J., and R. G. Dean (2003), Wave transformation by two-dimensional bathymetric anomalies with sloped transitions, *Coastal. Eng.*, *50*, 61–84, doi:10.1016/j.coastaleng.2003.08.002.

Booji, N. (1983), A note on the accuracy of the mild-slope equation, *Coastal Eng.*, *7*, 191–203.

Chanson, H., and J. S. Montes (1995), Characteristics of undular hydraulic jumps. Experimental apparatus and flow patterns, *J. Hydraul. Eng.*, *121*(2), 129–144.

D'Alpaos, A., S. Lanzoni, M. Marani, S. Fagherazzi, and A. Rinaldo (2005), Tidal network ontogeny: Channel initiation and early development, *J. Geophys. Res.*, *110*, F02001, doi:10.1029/2004JF000182.

D'Alpaos, A., S. Lanzoni, S. M. Mudd, and S. Fagherazzi (2006), Modeling the influence of hydroperiod and vegetation on the cross-sectional formation of tidal channels, *Estuarine Coastal Shelf Sci.*, *69*(3–4), 311–324, doi:10.1016/j.ecss.2006.05.002.

Day, J., L. Britsch, S. Hawes, G. Shaffer, D. Reed, and D. Cahoon (2000), Pattern and process of land loss in the Mississippi delta: A spatial and temporal analysis of wetland habitat change, *Estuaries*, *23*(4), 425–438, doi:10.2307/1353136.

Defina, A., L. Carniello, S. Fagherazzi, and L. D'Alpaos (2007), Self-organization of shallow basins in tidal flats and salt marshes, *J. Geophys. Res.*, *112*, F03001, doi:10.1029/2006JF000550.

Department of the Army, Waterways Experiment Station, Corps of Engineers, and Coastal Engineering Research Center (1984), *Shore Protection Manual*, vol. 1, 4th ed., 532 pp., Department of the Army, Waterways Experiment Station, Corps of Engineers, and Coastal Engineering Research Center, Washington, D. C.

Edinger, E., and D. R. Browne (2000), Continental seas of Western Indonesia, in *Seas at the Millennium: An Environmental Evaluation*, edited by C. Shepard, pp. 381–404, Elsevier Sci., Oxford, U. K.

Erduran, K. S., S. Ilic, and V. Kutija (2005), Hybrid finite-volume finite-difference scheme for the solution of Boussinesq equations, *Int. J. Numer. Meth. Fluids*, *49*, 1213–1232, doi:10.1002/fld.1021.

Fagherazzi, S., and D. J. Furbish (2001), On the shape and widening of salt marsh creeks, *J. Geophys. Res.*, *106*(C1), 991–1003.

Fagherazzi, S., and I. Overeem (2007) Models of deltaic and inner continental shelf landform evolution, *Annu. Rev. Earth Planet. Sci.*, *35*, 685–715.

Fagherazzi, S., and P. L. Wiberg (2009), Importance of wind conditions, fetch, and water levels on wave-generated shear stresses in shallow intertidal basins, *J. Geophys. Res.*, *114*, F03022, doi:10.1029/2008JF001139.

Fagherazzi, S., and T. Sun (2004), A stochastic model for the formation of channel networks in tidal marshes, *Geophys. Res. Lett.*, *31*, L21503, doi:10.1029/2004GL020965.

Fagherazzi, S., L. Carniello, L. D'Alpaos, and A. Defina (2006), Critical bifurcation of shallow microtidal landforms in tidal flats and salt marshes, *Proc. Natl. Acad. Sci. U. S. A.*, *103*(22), 8337–8341.

Fagherazzi, S., C. Palermo, M. C. Rulli, L. Carniello, and A. Defina (2007), Wind waves in shallow microtidal basins and the dynamic equilibrium of tidal flats, *J. Geophys. Res.*, *112*, F02024, doi:10.1029/2006JF000572.

Feagin, R. A. (2008) Vegetation's role in coastal protection, *Science*, *320*, 176–177.

Hibberd, S., and D. H. Peregrine (1979), Surf and run-up on a beach: A uniform bore, *J. Fluid Mech.*, *95*(2), 323–345.

Hu, K., C. G. Mingham, and D. M. Causon (1998), A bore-capturing finite volume method for open-channel flows, *Int. J. Numer. Meth. Fluids*, *28*, 1241–1261.

Karambas, T. V., and C. Koutitas (1992), A breaking wave propagation model based on the Boussinesq equations, *Coastal Eng.*, *18*, 1–19.

Karambas, T. V., and N. P. Tozer (2003), Breaking waves in the Surf and Swash Zone, *J. Coastal Res.*, *19*(3), 514–528.

King, S. E., and J. N. Lester (1995), The value of salt marshes as a sea defence, *Mar. Pollut. Bull.*, *30*(3), 180–189.

Kirby, J. T. (2003), Boussinesq models and applications to nearshore wave propagation, surfzone processes and wave-induced currents, in *Advances in Coastal Modeling*, vol. 67, edited by V. C. Lakhan, pp. 1–41, Elsevier Sci., Amsterdam, Netherlands.

Kirby, R. (2000), Practical implications of tidal flat shape, *Cont. Shelf Res.*, *20*, 1061–1077, doi:10.1016/S0278-4343(00)00012-1.

Kirwan, M. L., and A. B. Murray (2007), A coupled geomorphic and ecological model of tidal marsh evolution, *Proc. Natl. Acad. Sci. U. S. A.*, *104*(15), 6118–6122.

Kobayashi, N., G. S. DeSilva, and K. D. Watson (1989), Wave transformation and swash oscillation on gentle and steep slopes, *J. Geophys. Res.*, *94*(C1), 951–966.

Lamb, H. (1932), *Hydrodynamics*, 6th ed., 768 pp., Cambridge Univ. Press, Cambridge, U. K.

Lawson, S., P. Wiberg, K. J. McGlathery, and D. C. Fugate (2007), Wind-driven sediment suspension controls light availability in a shallow coastal lagoon, *Estuaries Coasts*, *30*(1), 102–112.

Lynett, P. J., and P. L.-F. Liu (2004), Linear analysis of the multilayer model, *Coastal Eng.*, *51*, 439–454, doi:10.1016/j.coastaleng.2004.05.004.

Lynett, P. J., T.-R. Wu, and P. L.-F. Liu (2002), Modeling wave runup with depth-integrated equations, *Coastal Eng.*, *46*, 89–107, doi:10.1016/S0378-3839(02)00043-1.

Madsen, P. A., and H. A. Schäffer (1999), A review of Boussinesq-type equations for gravity waves, in *Advances in Coastal and Ocean Engineering*, vol. 5, edited by P. L.-F. Liu, pp. 1–94, World Sci., Singapore.

Madsen, P. A., and O. R. Sørensen (1992), A new form of the Boussinesq equations with improved linear dispersion characteristics. Part 2: A slowly varying bathymetry, *Coastal Eng.*, *18*, 183–204, doi:10.1016/0378-3839(92)90019-Q.

Madsen, P. A., R. Murray, and O. R. Sørensen (1991), A new form of the Boussinesq equations with improved linear dispersion characteristics: Part 1, *Coastal Eng.*, *15*, 371–388.

Madsen, P. A., O. R. Sørensen, and H. A. Schäffer (1997), Surf zone dynamics simulated by a Boussinesq type model. Part I. Model description and cross-shore motion of regular waves, *Coastal Eng.*, *32*, 255–287.

Madsen, P. A., D. R. Fuhrman, and B. Wang (2006), A Boussinesq-type method for fully nonlinear waves interacting with a rapidly varying bathymetry, *Coastal Eng.*, *53*, 487–504, doi:10.1016/j.coastaleng.2005.11.002.

Mariotti, G., and S. Fagherazzi (2010), A numerical model for the coupled long-term evolution of salt marshes and tidal flats, *J. Geophys. Res.*, *115*, F01004, doi:10.1029/2009JF001326.

Möller, I. (2006), Quantifying saltmarsh vegetation and its effect on wave height dissipation: Results from a UK East coast saltmarsh, *Estuarine Coastal Shelf Sci.*, *69*, 337–351, doi:10.1016/j.ecss.2006.05.003.

Möller, I., and T. Spencer (2002), Wave dissipation over macro-tidal saltmarshes: Effects of marsh edge typology and vegetation change, *J. Coastal Res.*, *36*, 506–521.

Möller, I., T. Spencer, J. R. French, D. J. Leggett, and M. Dixon (1999), Wave transformation over salt marshes: A field and numerical modelling study from North Norfolk, England, *Estuarine Coastal Shelf Sci.*, *49*, 411–426, doi:10.1006/ecss.1999.0509.

Möller, I., J. Lendzion, T. Spencer, A. Hayes, and S. Zerbe (2009), The sea-defence function of micro-tidal temperate coastal wetlands, in *Coastal Processes*, vol. 126, edited by C. A. Brebbia, G. Benassai, and G. R. Rodriguez, pp. 51–62, WIT, Boston, Mass.

Morris, J. T., P. V. Sundareshwar, C. T. Nietch, B. Kjerfve, and D. R. Cahoon (2002), Responses of coastal wetlands to rising sea level, *Ecology*, *83*, 2869–2877.

Mudd, S. M., S. Fagherazzi, J. T. Morris, and D. J. Furbish (2004), Flow, sedimentation, and biomass production on a vegetated salt marsh in South Carolina: Toward a predictive model of marsh morphologic and ecologic evolution, in *The Ecogeomorphology of Tidal Marshes*, *Coastal Estuarine Stud.*, vol. 56, edited by S. Fagherazzi, M. Marani, and L. K. Blum, 266 pp., AGU, Washington, D. C.

Oertel, G. F. (2001), Hypsographic, hydro-hypsographic and hydrological analysis of coastal bay environments, Great Machipongo Bay, Virginia, *J. Coastal Res.*, *17*, 775–783.

Okamoto, T., and D. R. Basco (2006), The Relative Trough Froude Number for initiation of wave breaking: Theory, experiments and numerical model confirmation, *Coastal Eng.*, *53*, 675–690.

Pedersen, J. B. T., and J. Bartholdy (2007), Exposed salt marsh morphodynamics: An example from the Danish Wadden Sea, *Geomorphology*, *90*(1–2), 115–125.

Peregrine, D. H. (1966), Calculations of the development of an undular bore, *J. Fluid Mech.*, *25*(2), 321–330.

Peregrine, D. H. (1967), Long waves on a beach, *J. Fluid Mech.*, *27*, 815–827.

Peregrine, D. H., and I. A. Svendsen (1978), Spilling breaker, bores and hydraulic jumps, *Proc. 16th Int. Conf. Coastal Eng.*, *1*, 540–550.

Pringle, A. W. (1995), Erosion of a cyclic saltmarsh in Morecambe Bay, North-West England, *Earth Surf. Processes Landforms*, *20*(5), 387–405.

Pethick, J. S. (1981), Long-term accretion rates on tidal slat marshes, *J. Sediment. Petrol.*, *51*, 571–577.

Schäffer, H. A., and P. A. Madsen (1995), Further enhancements of Boussinesq-type equations, *Coastal Eng.*, *26*, 1–14.

Schäffer, H. A., P. A. Madsen, and R. Deigaard (1993), A Boussinesq model for waves breaking in shallow water, *Coastal Eng.*, *20*, 185–202.

Schwimmer, R. A. (2001), Rates and processes of marsh shoreline erosion in Rehoboth Bay, Delaware, U.S.A., *J. Coastal Res.*, *17*(3), 672–683.

Suh, K. D., C. Lee, and W. S. Park (1997), Time-dependent equations for wave propagation on rapidly varying topography, *Coastal Eng.*, *32*, 91–117.

Silvestri, S., A. Defina, and M. Marani (2005), Tidal regime, salinity and salt marsh plant zonation, *Estuarine Coastal Shelf Sci.*, *62*, 119–130, doi:10.1016/j.ecss.2004.08.010.

Soares Frazão, S., and Y. Zech (2002), Undular bores and secondary waves—Experiments and hybrid finite-volume modelling, *J. Hydraul. Res.*, *40*, 33–43.

Stive, M. J. F. (1980), Velocity and pressure field of spilling breakers, *Proc. 17th Int. Conf. Coastal Eng.*, *1*, 547–566.

Temmerman, S., G. Govers, S. Wartel, and P. Meire (2004), Modelling estuarine variations in tidal marsh sedimentation: Response to changing sea level and suspended sediment concentrations, *Mar. Geol.*, *212*, 1–19.

Tonelli, M., and M. Petti (2009), Hybrid finite volume—finite difference scheme for 2DH improved Boussinesq equations, *Coastal Eng.*, *56*, 609–620, doi:10.1016/j.coastaleng.2009.01.001.

Tonelli, M., and M. Petti (2010), Finite volume scheme for the solution of 2D extended Boussinesq equations in the surf zone, *Ocean Eng.*, *37*, 567–582, doi:10.1016/j.oceaneng.2010.02.004.

Toro, E. F. (2001), *Shock-Capturing Methods for Free-Surface Shallow Flows*, 326 pp., John Wiley, West Sussex, U. K.

van de Koppel, J., D. van der Wal, J. P. Bakker, and P. M. J. Herman (2005), Self-organization and vegetation collapse in salt marsh ecosystems, *Am. Naturalist*, *165*, E1–E12.

van der Wal, D., and K. Pye (2004), Patterns, rates and possible causes of saltmarsh erosion in the Greater Thames area (UK), *Geomorphology*, *61*, 373–391.

Veeramony, J., and I. A. Svendsen (2000), The flow in surf-zone waves, *Coastal Eng.*, *39*, 93–122.

Watson, G., and D. H. Peregrine (1992), Low frequency waves in the surf zone, *Proc. 23rd Int. Conf. Coastal Eng.*, 818–831.

Wei, G., and J. T. Kirby (1995), Time-dependent numerical code for extended Boussinesq equations, *J. Waterw. Port Coastal Ocean Eng.*, *121*, 251–261.

Zelt, J. A. (1991), The run-up of non-breaking and breaking solitary waves, *Coastal Eng.*, *15*, 205–246.

Zhou, J. G., D. M. Causon, C. G. Mingham, and D. M. Ingram (2001), The surface gradient method for the treatment of source terms in the shallow-water equations, *J. Comput. Phys.*, *168*, 1–25.

S. Fagherazzi and M. Tonelli, Department of Earth Sciences and Center for Computational Science, Boston University, 675 Commonwealth Ave., Boston, MA 02215, USA. (mara.tonelli@uniud.it)

M. Petti, Dipartimento di Georisorse e Territorio, Università degli Studi di Udine, via del Cotonificio 114, I-33100 Udine, Italy.